We are IntechOpen,
the world's leading publisher of
Open Access books
Built by scientists, for scientists

6,900
Open access books available

186,000
International authors and editors

200M
Downloads

Our authors are among the

154
Countries delivered to

TOP 1%
most cited scientists

12.2%
Contributors from top 500 universities

CLARIVATE ANALYTICS
BOOK CITATION INDEX
INDEXED

WEB OF SCIENCE™

Selection of our books indexed in the Book Citation Index
in Web of Science™ Core Collection (BKCI)

Interested in publishing with us?
Contact book.department@intechopen.com

Solid-Phase Crystallization of Amorphous Silicon Films

Dong Nyung Lee and Sung Bo Lee

Additional information is available at the end of the chapter

1. Introduction

Polycrystalline silicon thin-film transistors (poly-Si TFTs) have recently attracted considerable attention for their high field-effect mobility and response velocity [1,2]. For low fabrication cost, poly-Si TFTs should be made on inexpensive glass substrates. In order to lower the crystallization temperature of amorphous silicon (*a*-Si) below the intrinsic crystallization temperature (~600 ºC), effects of metal impurities on crystallization have been investigated using Au [3], Al [4], and Sb [5] forming eutectics with Si, and Pd [6] and Ni [7] forming silicides with Si. This process is referred to as metal-induced crystallization (MIC). Following the MIC, its variants, such as the metal-induced lateral crystallization (MILC) [8] and the field-aided lateral crystallization (FALC) [9–12], have been introduced as attempts to lower crystallization temperature and to reduce the contamination by a metal catalyst. For the MILC process, the flux of the diffusing species is governed only by the concentration gradient, but for the FALC process, the flux can be affected by not only the concentration gradient but also the applied electric potential gradient. In the FALC process, the crystallization front typically migrates from the negative electrode side to the positive electrode side. In the FALC, the application of a DC electric field increases the crystallization rate, as compared with the MILC (without any electric field) and MIC. In the FALC process, Ni and Cu, both of which are silicide forming metals, have been reported to produce high crystallization rates [12]. The mechanism of the crystallization induced by Ni was examined in detail by Hayzelden and his coworkers [13, 14] using *in situ* transmission electron microscopy (TEM) and high-resolution TEM.

The *a*-Si films are generally deposited on glass by physical or chemical vapor deposition. When annealed, they undergo crystallization by nucleation and growth. For the solid-phase crystallization of *a*-Si films on glass by heating, the directed crystallization, in which crystallization is favored in special crystallographic directions of crystallites, is not easily expected because both *a*-Si and glass are physically isotropic. However, the directed crystallization is rather general in the solid-phase crystallization of *a*-Si on glass at low temperatures [8,15–19]. Lee et

al. [8] advanced a model for the directed crystallization and later the model was further refined [20,21]. The model is introduced and is applied to the solid-phase epitaxial growth rate of c-Si in self-implanted Si(100) wafer, the solid-phase epitaxial growth rate of c-Si in self-implanted Si(100) wafer [22,23], the metal-induced crystallization of a-Si film on glass, and the silicide mediated crystallization.

2. Directed crystallization theory

The solid-phase transformation of a metastable amorphous material into a crystal, or the solid-phase crystallization of an amorphous material, needs the activation energy. The energy is usually supplied in the form of thermal energy by increasing the temperature of the material. When the nucleation occurs, the strain energy develops in the amorphous matrix as well as in the crystallites. The strain energy may be referred to as the accommodation strain energy. The strain energy is likely to give rise to inhomogeneous growth rates of crystallites due to their elastic anisotropy, if any. We discuss the evolution of the strain energy qualitatively [20,21].

The stress state of thin film deposits can be approximated by plane stress because the principal stress normal to the film surface is negligibly small compared with those along the surface. We consider a circular disk cut from a large, elastically isotropic metastable-phase sheet. When the disk is transformed into its stable phase, its dimension is likely to differ from the original diameter of the metastable phase due to a difference in density between the two phases. If the stable phase is elastically isotropic, the stable disk will be circular. When the density of the stable phase is higher than that of the metastable phase, the diameter of the stable-phase disk is smaller than that of the metastable phase, and vice versa. When the ends of the two phases are pulled toward each other and joined together, the strain and stress fields develop in the both phases.

In order to obtain the stress distribution of this system, we first adopt the solution of the stress distribution in a hollow cylinder subjected to uniform pressure on the inner and outer surfaces (Figure 1). The solution of this problem is due to Lamé and expressed as follows [22]:

$$\sigma_r = \frac{a^2 b^2 (p_o - p_i)}{(b^2 - a^2) r^2} + \frac{p_i a^2 - p_o b^2}{b^2 - a^2} \tag{1}$$

$$\sigma_\theta = -\frac{a^2 b^2 (p_o - p_i)}{(b^2 - a^2) r^2} + \frac{p_i a^2 - p_o b^2}{b^2 - a^2} \tag{2}$$

where σ_r and σ_θ denote the normal stress components in the radial and circumferential directions, and p_i and p_o the uniform internal and external pressures. Other symbols are defined in Figure 1. This solution is useful because it gives the stress distribution in the region

of $a < r < b$, which may be equivalent to the metastable region in the present case. When the cylinder is subjected to internal pressure only, $p_o = 0$, with $b \gg a$, Eqs. 1 and 2 give

$$\sigma_r = \frac{a^2 p_i}{b^2}\left(1 - \frac{b^2}{r^2}\right) \tag{3}$$

$$\sigma_\theta = \frac{a^2 p_i}{b^2}\left(1 + \frac{b^2}{r^2}\right) \tag{4}$$

These equations show that σ_r is always a compressive stress and σ_θ a tensile stress. If the cylinder is subjected to uniform internal tensile stress only, $p_i < 0$, σ_r is always a tensile stress and σ_θ a compressive stress. This is relevant to the case when the density of the stable phase is higher than that of the metastable phase, as in crystallization of a-Si. The magnitude of σ_r and σ_θ are maxima at $r = a$, decreasing with increasing r regardless of internal pressure or internal tensile stress.

When the stable phase is elastically anisotropic, the pulling displacement of the circumference of the stable phase depends on its stiffness, the stiffer the smaller displacement at a given force. The smaller displacement of the stable phase requires the larger pulling displacement of the metastable phase, which induces the higher strain energy in the metastable phase.
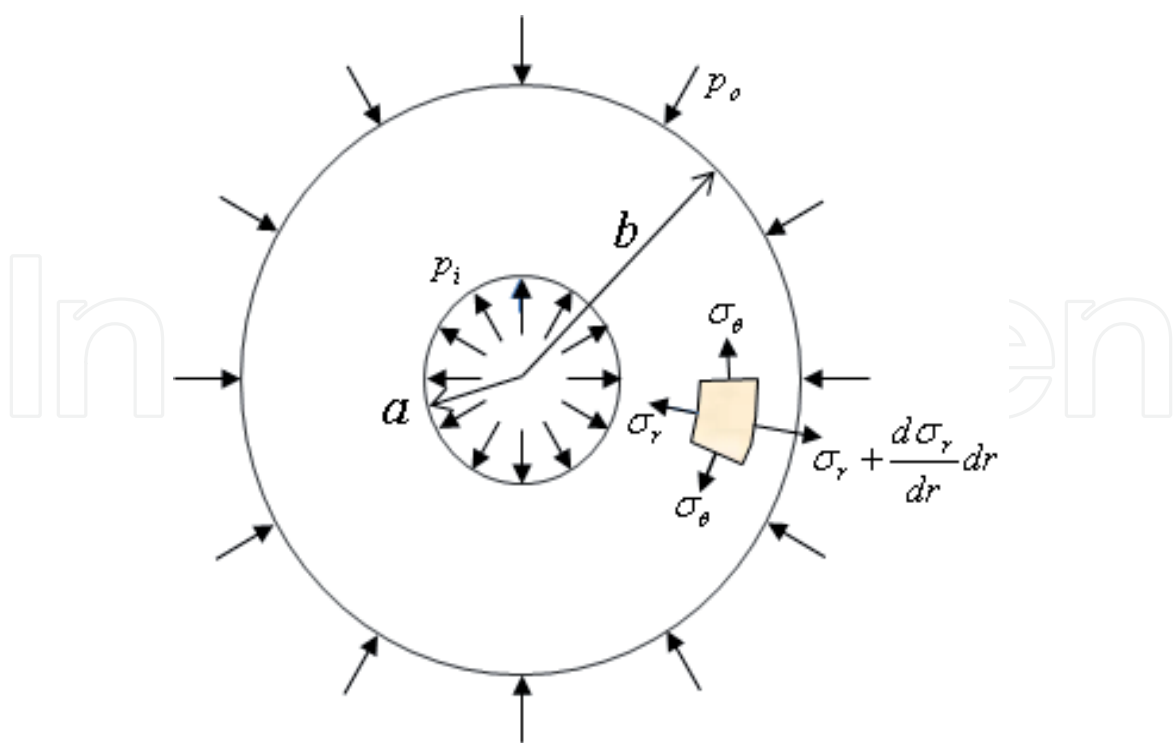

Figure 1. Hollow cylinder subjected to uniform pressure.

A qualitative account of this can be made using rectangular elements shown in Figure 2(a). The elements may be approximated by uniaxial specimens with fixed ends as shown in Figure 2(b). Let the metastable phase be elastically isotropic and its stiffness be C_m. If the stable phase is an elastically anisotropic single crystal, its stiffness is likely to vary with its crystallographic direction. C_h and C_l denote the stiffnesses of elements along different crystallographic directions of the stable phase, with $C_h > C_l$. The force F_1 for joining the specimen of C_l to that of C_m can differ from the force F_2 for joining the specimen of C_h to that of C_m.

(a)   (b)   (c)
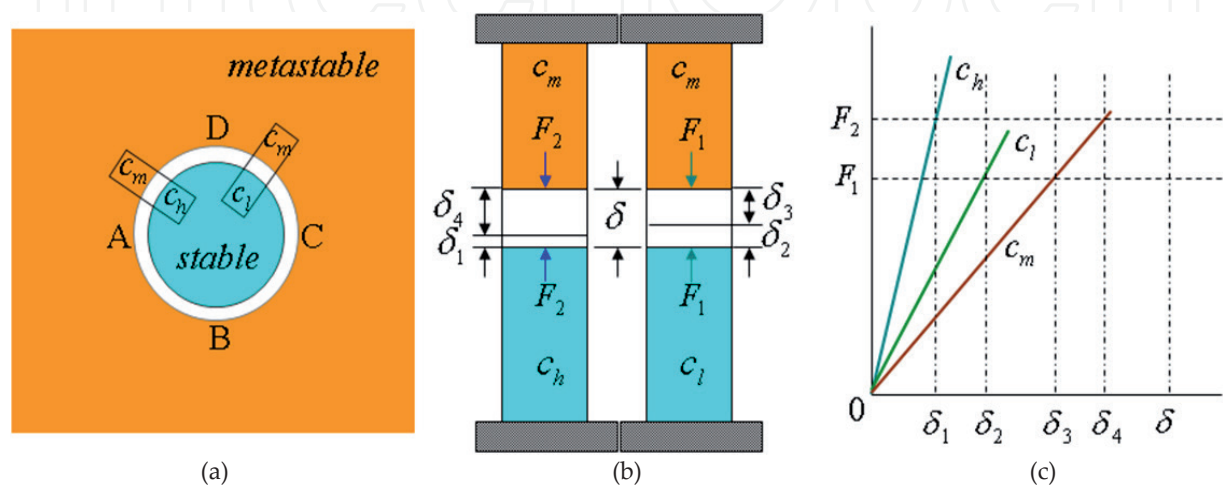
Figure 2. (a) Gap generated after circular metastable-phase ABCD is transformed into stable phase without generating stresses, when density of stable phase is higher than that of metastable phase, and hypothetical rectangular elements with different stiffness values. C_m is stiffness of metastable phase, and C_h and C_l are stiffnesses of stable phase with $C_h > C_l$. (b) Elements in (a) acting as tensile specimens with fixed ends. (c) Forces F_i and displacements δ_j necessary to join ends of metastable-phase and stable-phase specimens [21].

From Figure 2(c), we can obtain the following relations.

$$C_l = F_1 / \delta_2 \tag{5}$$

$$C_h = F_2 / \delta_1 \tag{6}$$

$$C_m = F_1 / \delta_3 = F_2 / \delta_4 \tag{7}$$

$$\delta = \delta_1 + \delta_4 = \delta_2 + \delta_3 \tag{8}$$

It follows from the above relations that

$$\left(C_m / C_h + 1\right)\delta_4 = \left(C_m / C_l + 1\right)\delta_3 \tag{9}$$

Since $C_h > C_l$, Eq. 9 gives $\delta_4 > \delta_3$ and hence we obtain $F_2 > F_1$ from Eq. 7.

The strain energy of the metastable phase adjacent to the stable phase with C_h is given by

$$W_2 = F_2 \delta_4 / 2 \qquad (10)$$

Similarly, that of the metastable phase adjacent to the stable phase with C_l is given by

$$W_1 = F_1 \delta_3 / 2 \qquad (11)$$

Since $\delta_4 > \delta_3$ and $F_2 > F_1$, we obtain $W_2 > W_1$. In other words, the metastable phase is subjected to the higher strain energy in the higher stiffness direction of the stable phase.

The stiffness C is related to Young's modulus E as $C = EA/L$ with A and L being the cross-sectional area and the length of the stable-phase element, respectively. Therefore, it can be stated that the highest strain-energy density region in the metastable phase containing a stable phase crystallite is the stable/metastable interface region in the highest Young's modulus directions of the stable phase. As the heating temperature increases, the strain energy contribution to the activation energy for continuing crystallization will decrease [21].

For a thin amorphous deposit, another form of strain energy can develop due to a difference in thermal expansion coefficient between the deposit and the substrate in addition to the accommodation strain energy. The strain energy is termed the thermal strain energy. The thermal stress developed in the thin deposit, which is associated with the thermal strain energy, is equivalent to an external stress along the surface. If the stress is planar isotropic, the directed crystallization is unlikely to occur along the deposit surface in the absence of the accommodation strain energy. However, the stress can influence the crystal growth rate.

3. Solid-phase epitaxial growth rate of crystalline Si in self-implanted Si(100) wafer

3.1. Uniaxial stress ranged from — 0.55 to 0.55 GPa

The a-Si/c-Si interface region is under the tensile stress because the density of c-Si is higher than that of a-Si (Section 4). According to Section 2, if the tensile stress in specimen is increased by external tensile forces, the strain energy in the interface region will increase, which in turn will increase the crystallization rate, and vice versa.

Aziz et al. [23] studied the solid-phase epitaxial growth rate of c-Si from a-Si by bending bar-shaped Si(001) wafers with a three-point bending system at about 540 °C. The Si wafers (p type, 1 ohm cm, 0.84 mm thickness) were implanted on both sides at 77 K with ^{30}Si$^+$ (60 keV, 1×10^{15} cm^{-2}; 180 keV, 2×10^{15} cm^{-2}) to create 280-nm-thick amorphous surface layers. The wafers were diced into bars >20 mm in length in the [110] direction by 5 mm in width.

One side of the elastically bent specimen is approximately under a uniaxial tensile stress state and the other side under a uniaxial compressive stress state, in which the stress ranged from –0.55 GPa (compressive) to 0.55 GPa (tensile). Their measured crystallization rate as a function of applied stress showed that the rate in the tension side was higher than that in the compression side. Aziz et al. claimed that the stress existed in the crystal at the crystalline-amorphous interface because there is no stress in the bulk of the *a*-Si due to stress relief by viscous flow [24]. Even though the initial stress in the *a*-Si could be completely relieved during the stress measurement, the stress developed in the *a*-Si at the *c*-Si/*a*-Si interface during crystallization might not be removed immediately.

Even if we cannot distinguish the initial stress from the stress developed during crystallization, it is apparent that the *a*-Si film on the tension side of the sample could be more stressed in tension than that on the compression side. Therefore, we can expect that the grain growth rate in the film on the tension side will be higher than that in the film on the compression side in agreement with the measured data.

3.2. Effect of hydrostatic pressure up to 3.2 GPa

Lu et al. [25] measured the hydrostatic pressure dependence of the solid-phase epitaxial growth rate of self-implanted Si(100) by using the in situ time-resolved interferometric technique and high-pressure diamond anvil cell. With fluid argon as the pressure transmission medium, a hydrostatic pressure environment was achieved around the sample. The external heating geometry employed provided a uniform temperature across the sample. At temperatures of 530–550 °C and pressures up to 3.2 GPa, the growth rate was enhanced by up to a factor of 5 over that at 1 atmosphere pressure ($\approx$ 0.1 MPa).

This result appears to contradict the non-hydrostatic stress effect explained in Section 3.1. The crystallization of *a*-Si results in a decrease in volume. Therefore, a hydrostatic compression is expected to accelerate crystallization. We roughly estimate a hydrostatic pressure for the crystallization of *a*-Si without taking the thermal activation into account.

Let P and Δ denote the hydrostatic pressure and the volumetric dilatation for crystallization of *a*-Si, respectively. The pressure is related to the dilatation as follows:

$$P = -B\Delta \tag{12}$$

where B is the bulk modulus of *a*-Si and the volumetric dilatation Δ is defined as

$$\Delta = \frac{V - V_0}{V_0} \tag{13}$$

Here V_0 is the volume before crystallization, and V is the volume after crystallization. The density of *c*-Si at room temperature is 2320 to 2340 kg m^{-3} [26]. If the density of *c*-Si is set to be

2330 kg m^{-3}, the specific volume of c-Si is calculated to be 4.29×10^{-4} m^3 kg^{-1}. Ion-implanted amorphous silicon is 1.8% less dense than c-Si at room temperature [27]. Therefore, the density of a-Si at room temperature is calculated to be 2288 m^3 kg^{-1} and its specific volume is calculated to be 4.37×10^{-4} m^3 kg^{-1}. Since the volumes of a-Si and c-Si vary with temperature, we calculate those at 540 °C. The linear thermal expansion coefficients of a-Si and c-Si are almost the same, about 3×10^{-6} K^{-1} [24, 28]. Therefore, the specific volume of a-Si at 540 °C is 4.39×10^{-4} m^3 kg^{-1} {= $4.37 \times 10^{-4} \times [1+3 \times 3 \times 10^{-6} \times (540-25)]$}, and that of c-Si at 540 °C is 4.31×10^{-4} m^3 kg^{-1} {= $4.29 \times 10^{-4} \times [1+3 \times 3 \times 10^{-6} \times (540-25)]$}. The volumetric dilatation at 540 °C is

$$\Delta = \left(4.31 - 4.39\right)/4.39 = -0.0182. \tag{14}$$

For lack of the bulk modulus of a-Si at 540 °C, it has been calculated using the biaxial modulus of ion-beam-sputtered a-Si at 110 °C, M_σ (110) = 140 GPa [24], the temperature dependence of M for Si(100) [24], and Poisson's ratio ν of a-Si film deposited by rf sputtering onto Si substrate in an atmosphere of $P_{H_2}/(P_{H_2}+P_{Ar}) = 0.001$ [29]. The bulk modulus B and the biaxial modulus M_σ can be expressed as

$$B = \frac{E}{3(1-2\nu)} \tag{15}$$

$$M_\sigma = \frac{E}{(1-\nu)} \tag{16}$$

where E is Young's modulus. The temperature dependence of M_σ(T) for Si(100) is given by

$$\frac{d\ln M_\sigma(\text{T})}{dT} = -62 \times 10^{-6} \text{K}^{-1}$$

From this we obtain M_σ (540) = 136 GPa. According to Jiang et al. [29], $\nu = 0.32$. Substitution of M_σ (540) = 136 GPa and $\nu = 0.32$ into Eq. 16 gives E (540) = 92.5 GPa. In this calculation, Poisson's ratio was assumed to be independent of temperature. From these elastic constants, the bulk modulus of a-Si at 540 °C, B (540) = 85.6 GPa, is obtained. Therefore, the hydrostatic pressure for crystallization at 540 °C is calculated as P (540) = 1.56 GPa. From this estimation we can see that hydrostatic pressures of the order of GPa will accelerate the crystal growth rate.

Stresses of the order of 0.1 GPa in Section 3.1 are too low to be effective in the grain growth of c-Si. On the other hand, its contribution to the local tensile stress developed in the a-Si/c-Si interface could be much higher. Therefore, the compressive stresses of the order of 0.1 GPa reduced the growth rate, and the tensile stresses increased the growth rate.

4. Crystallization of amorphous Si on glasses

According to the directed-growth theory described in Section 2, the highest crystallization rate would be along the maximum Young's modulus direction (MxYMD). In order to understand crystallization anisotropy of a-Si, we need to calculate Young's modulus of crystalline Si (c-Si). Young's modulus E for crystals of cubic system is given by Eq. 17 [30,31].,

$$1 / E = S_{11} + [S_{44} - 2(S_{11} - S_{12})](a_{11}^2 a_{12}^2 + a_{12}^2 a_{13}^2 + a_{13}^2 a_{11}^2) \qquad (17)$$

where S_{11}, S_{44}, and S_{12} are the compliances referred to the symmetric axes and a_{1i} are the direction cosines of the uniaxial stress direction 1 referred to the symmetric axes i. For the [hkl] direction,

$$\alpha_{11} = h / \sqrt{h^2 + k^2 + l^2}, \alpha_{12} = k / \sqrt{h^2 + k^2 + l^2}, \alpha_{13} = l / \sqrt{h^2 + k^2 + l^2} \qquad (18)$$

For silicon at 293 K, $S_{11} = 0.007685$, $S_{12} = -0.002139$, and $S_{44} = 0.01256$ GPa^{-1} [32], and [$S_{44} - 2 (S_{11} - S_{12})$] = -0.00708 <0. Therefore, the maximum and minimum values of ($a_{11}^2 a_{12}^2 + a_{12}^2 a_{13}^2 + a_{13}^2 a_{11}^2$) in Eq. 17 are 1/3 for the <111> directions and 0 for the <100> directions, respectively. Therefore, the growth rate of c-Si is likely to be the highest in the <111> directions.

For a-Si film/SiO$_2$ glass-substrate structure, the thermal strain-energy is the highest near the interface between the film and the substrate, or in the deepest place of the a-Si film, which is under the highest compressive stress because the thermal expansion coefficient of Si is higher than that of the SiO$_2$ layer. At low temperatures, crystallization of a-Si is likely to be dominated by the accommodation strain-energy along with the thermal strain energy. In this case, crystallization is likely to start near the film/substrate interface and the highest growth directions (the <111> directions) tend to be parallel to the surface because the film stress is the highest along the film/substrate interface or the surface.

Because the thickness of the Si film including a-Si and c-Si is much smaller than the dimensions along the film surface, the stress in the thickness direction is negligible, and the film is approximately under the plane stress state. That is, the film stress is the highest along the interface or the film surface. Therefore, when the <111> directions are placed along the film surface, the growth rate of crystallites will be the highest.

Let two of four <111> directions, for example, the [111] and [–1 1 1] directions be placed along the surface, then the thickness direction becomes the [0–1 1] direction (110 projection in Figure 3). Thus, the texture of crystallites is approximated by the <110>//ND (ND: the surface normal direction) orientation with the <111> branches. When three of the <111> directions are at 19.4° to the film/substrate interface and one of the <111> directions is parallel to the thickness direction [(111) projection in Figure 3], the <111>//ND texture can be obtained. This possibility is based on the relatively small angle of 19.4°. The directed crystallization can give rise to the dendritic

growth of crystallites. As the annealing temperature increases, the strain energy contribution decreases and the thermal energy becomes dominant. In this case, the directed crystallization will be suppressed, resulting in equiaxed crystallization and random orientation.
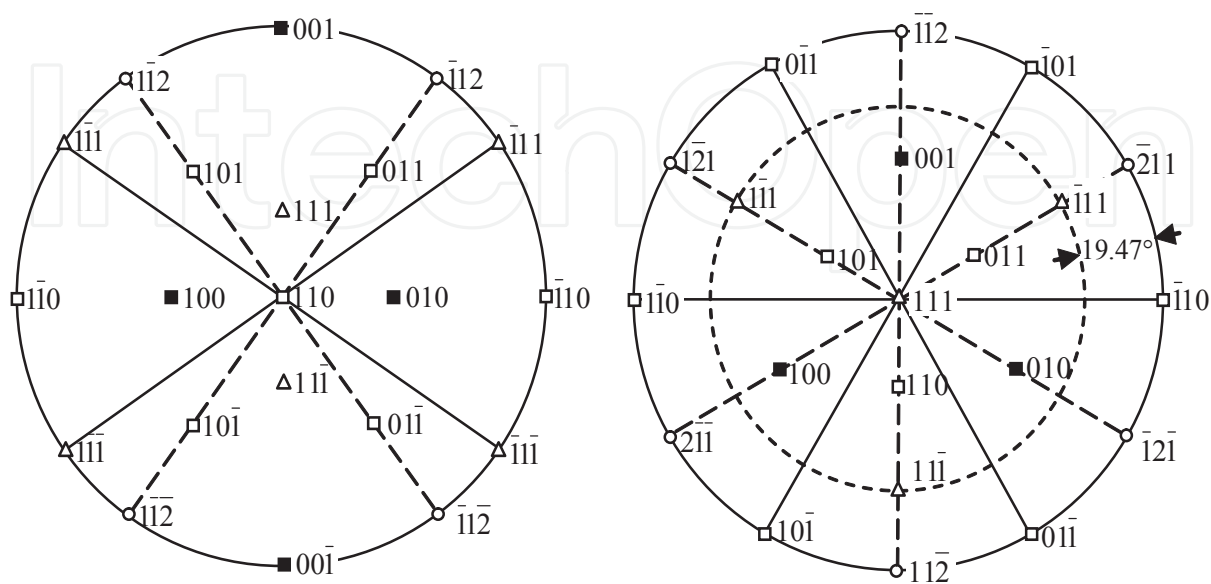

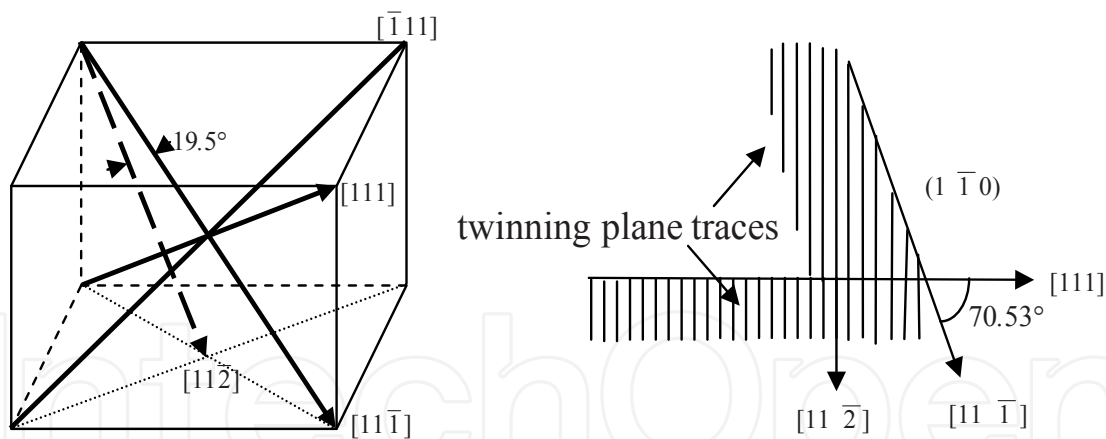**Figure 3.** Cubic (110) and (111) stereographic projections [21].

Figure 4. Twinning plane traces in [1–1 0]//ND oriented dendritic crystal whose branches are directed along [111] and [1 1–1] directions [20].

When the annealing temperature is high enough to activate the volume diffusion, the random orientation will change to the <111> texture because the {111} planes have the minimum surface energy density, to reduce the surface energy which is the major energy source in thin films. The <110> or <111> to random transition temperature or the random to <111> transition temperature is likely to decrease with increasing purity of Si films.

Silicon has a stacking-fault energy of about 50 mJ/m^2. This relatively small energy generates many twins during crystallization. The twinning planes and directions of c-Si are {111} and

<112>. Figure 4 shows the [1 1–2] twinning direction and twinning-plane traces in the [1–1 0]// ND oriented dendritic crystal whose branches are directed along the [111] and [1 1–1] directions. The angle between the [1 1–2] and [1 1–1] directions can appear smaller than 19.5°, when the specimen is slightly rotated about the [1 1–2] axis. This may make crystallites appear to grow along the <112> directions.
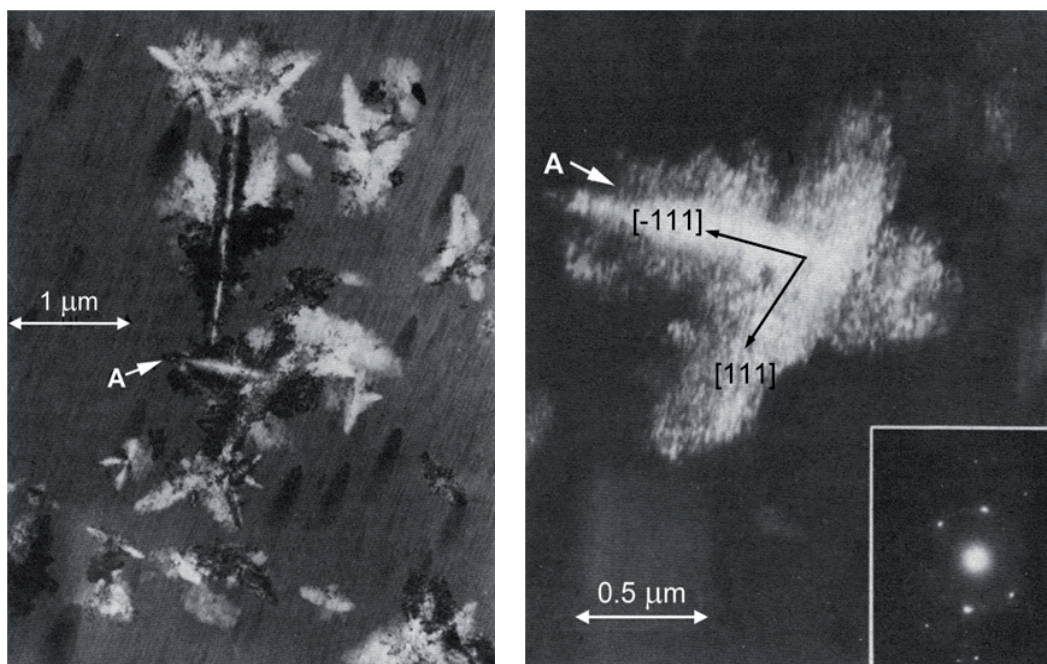
4.1. Evaporation-deposited *a*-Si films

Table 1 summarizes deposition conditions of a few *a*-Si films and their annealing textures. When heated at 650 °C for 1 h in flowing nitrogen in an open tube furnace, Si dendrites were observed. The selected area diffraction pattern of a dendrite indicated that dendrite arms were parallel to the <111> directions (Figure 5). The [1 1–1] was erroneously indexed as the [0 1–1] in [15]. When the heat-treatment temperature was raised to 850 °C, the film fully crystallized with equiaxed grains of 640 nm in normal mean size and dendrite remnants. The texture of the film was random. After heating at 1040 °C, the film had a microstructure consisting solely of equiaxed grains without dendrite remnants. The normal mean grain size for this film was 205 nm, and the texture of the film was random. The result is compatible with the prediction of the directed crystallization theory because the strain energy contribution to the activation energy decreases with increasing annealing temperature and in turn the anisotropic crystallization rate decreases [20].

film-thickness; deposition method	substrate	evapor. press. [Torr]	substr. temp. [°C]	deposit. rate [nm /min]	anneal. ambient	anneal. time. [h]	anneal. temp. [°C]	anneal. texture	Ref.
900 nm; evapor.	370 nm SiO$_2$ on <100> p-type Si	10^{-6}	300	300	Flowing N$_2$	1	650 850 1040	<110> random random	15
500 nm; evapor.	fused silica	base press. 10^{-10}	380	6	UHV or flowing N$_2$		600 700	random <111>	16
~100 nm; LPCVD 70 nm; Dose	glass		550		CF RTP RTP RTP CF	3 3 min 1 min 1 min 64	610 650 750 850 600	<110> <110> <110> <110> <111>	18

deposit.: deposition; evapor.: evaporation; substr.: substrate; temp.: temperature; anneal.: annealing;

CF: conventional furnace; RTP: rapid thermal process; Dose: implanted by a dose of 5×10^{15} cm^{-2} Si$^+$

at 30 keV; UHV: ultrahigh vacuum.

Table 1. Deposition conditions of *a*-Si films and their annealing textures

Whenever contamination is avoided prior to annealing under ultrahigh vacuum, crystallization occurred at 600 °C regardless of the substrate temperature in evaporation and the crystallized films had no texture [16]. They attributed the random orientation to the existence of voids in the amorphous films. However, the amorphous phase itself can give rise to the randomness at the absence of strain energies. The voids can reduce the strain energy of films, which in turn may enhance the random orientation. After annealing at 700 °C, the <111>//ND texture was obtained. In Anderson's work [15], the random orientation was obtained at 850 °C or 1040 °C and the <111>//ND texture was not observed within the experimental range. The differences are caused by differences in purity of the samples. Films obtained at lower pressures are likely to have higher purity. It is well known that the higher purity gives rise to the lower crystallization temperature.

Figure 5. Dendritic *c*-Si nucleating in evaporated *a*-Si film and dark-field image of dendrite at A (Experimental results [15]).

4.2. Amorphous $Si_{1-x}Ge_x$ films on SiO_2

Hwang et al. [19] deposited a-$Si_{1-x}Ge_x$ films with x = 0–0.53 on thermally oxidized Si<100> wafers by molecular beam epitaxy. The nominal thickness of the film was 100 nm and the deposition temperature was 300 °C. The base pressure and the deposition pressure were 10^{-10} Torr and 10^{-9} Torr, respectively, and the deposition rate was about 3 nm/min. When annealed at 600 °C, a-Si film (x = 0) crystallized into dendritic forms similar to Figure 5 with a strong <111>//ND texture. As the Ge concentration, or x, increased, the relative intensity of the (111) peak decreased. Figure 6 shows TEM micrographs of $Si_{0.47}Ge_{0.53}$ films annealed at 550 °C. From x-ray diffraction results, the texture of the film could be approximated by random orientation, when thickness factors were not taken into account.

When thickness factors are taken into account, its texture could be approximated by <110> +<311>//ND. Even though the accurate texture of the films cannot be obtained by this method, the texture of the films could be approximated by random orientation with weak <110>//ND and <311>//ND components. The near-spherical crystallites and the near-random texture seem be related to an increased contribution of the thermal energy. The solidus temperature of $Si_{0.47}Ge_{0.53}$ is 1095 °C, which is lower than the melting point of Si, 1414 °C (Figure 7). Therefore, at an annealing temperature of 600 °C, crystallization of $Si_{0.47}Ge_{0.53}$ was dominated by the thermal energy. The aspect ratio of crystallites decreased with increasing content of Ge [19]. This also reflects an increase in thermal energy contribution with increasing Ge content. The grain size in fully crystallized Si-Ge films decreased with increasing Ge content. The crystal structures, lattice parameters, intrinsic stacking-fault energy, and elastic anisotropies of Ge and Si are similar, and so the characteristics of the Ge-Si alloys are likely to be similar to those of Ge and Si. Therefore, for a given annealing temperature T, the decrease in the solidus temperature is equivalent to an increase in T/T_m, with T_m being the absolute melting point of a reference material (*eg*. Ge or Si) in the Ge–Si system.
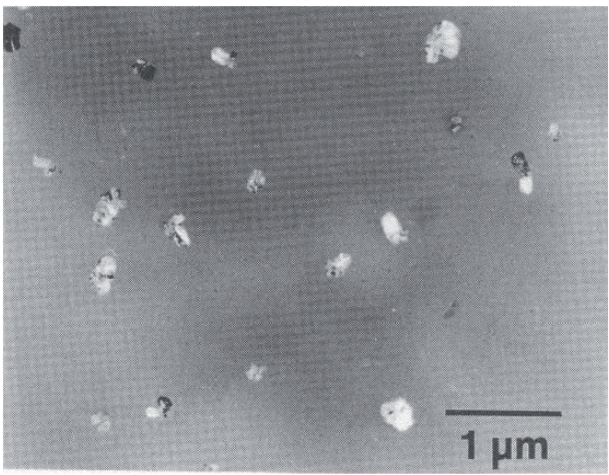
Figure 6. TEM of a-$Si_{0.47}Ge_{0.53}$ film after annealing at 550°C for 10 min [19].

The grain size G is likely to be reciprocally proportional to the nucleation rate dN/dt. Since the nucleation is a thermally activated process, the grain size and the nucleation rate can be expresses as

$$A/G = dN/dt = B\exp(-\frac{Q}{RT}) \tag{19}$$

where A and B are constants, and Q is the activation energy for nucleation. Therefore, we obtain

$$G = C\exp(\frac{Q}{RT}) \text{ or } \ln G = C_0 + \frac{Q}{RT} \text{ or } \ln G = C_0 + \frac{Q/T_m}{RT/T_m} \tag{20}$$
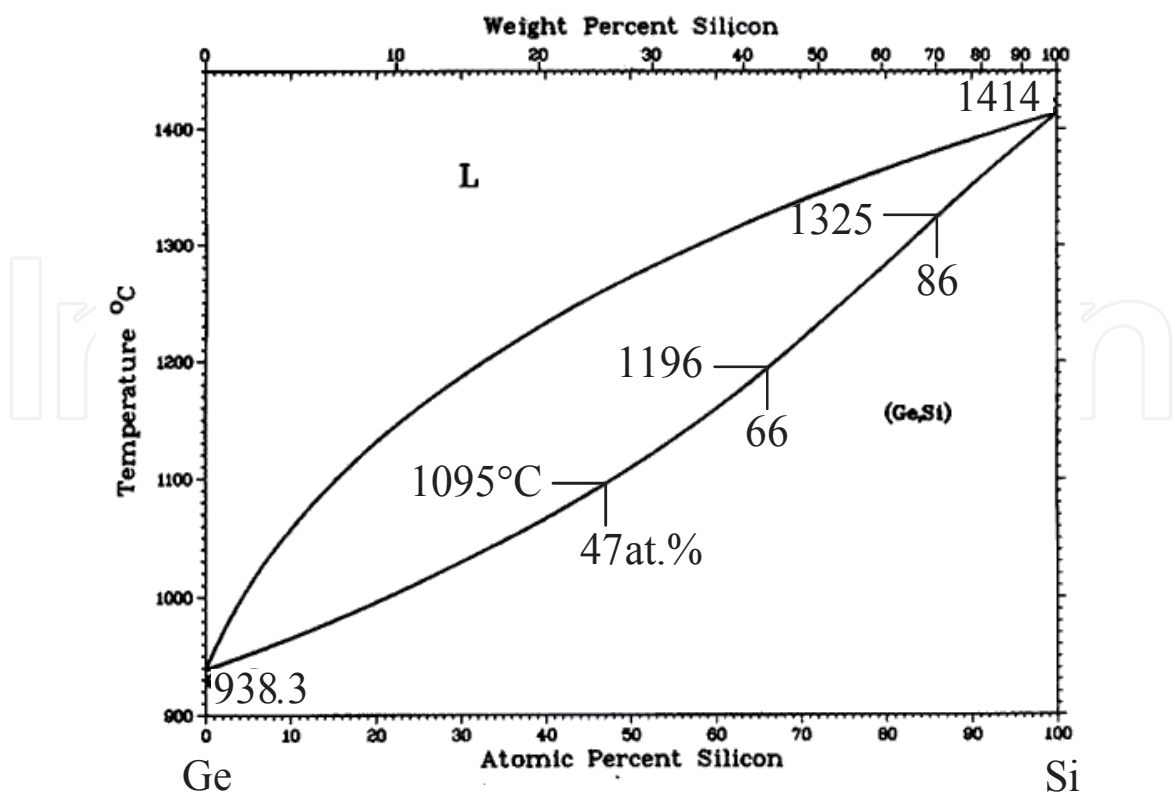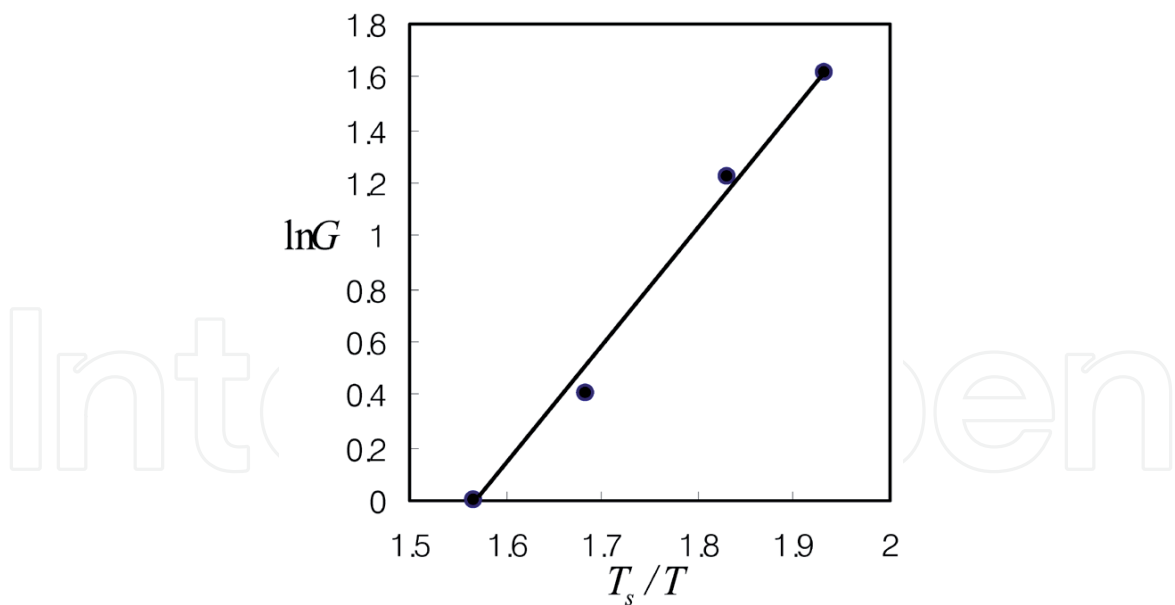
Figure 7. Ge–Si phase diagram [20]

Figure 8. Relationship between ln G and T_s/T [20].

where C (= A/B) and C_0 (=ln C) are constants. As discussed above, T/T_m can be assumed to be proportional to T/T_s, with T_s being the solidus temperatures of the Ge–Si system. Then Eq. (20) can be expressed as

$$\ln G = C_0 + \frac{Q}{RT} = C_0 + \frac{Q_0 T_s}{RT} \tag{21}$$

Here Q_0 (= Q/T_m) is a constant. The relationship between ln G and T_s/T is plotted in Figure 8. The good linear relationship in the figure supports the above assumption.

5. Metal-induced crystallization

5.1. Copper-induced crystallization

Lee et al. [8] deposited an 80 nm a-Si on Corning 1737 glass by plasma-enhanced chemical vapor deposition (PECVD) at 280ºC using Si_2H_6 and H_2 as source gases. The wafer was cut into 3×3 cm^2 square specimens for the subsequent process. To deposit copper on the a-Si film, the photoresist (PR) was spin-coated and patterned by a photolithographic process using rectangular mask patterns of 60×30 μm^2. A copper layer of 2 nm in thickness was deposited in a DC sputtering system. Copper on the PR patterns was removed by the lift-off method and only that deposited on the a-Si was left. The crystallization annealing was done at 500°C for 1 h in N_2 ambience. During the crystallization annealing an electric field of 1.80 kV/m was applied to the above metal-deposited specimen by the DC power supply.

From the crystallized specimen, 3 mm disks were cut using an ultrasonic cutter for TEM specimen preparation. For the plan-view studies of the a-Si film, the disks were mechanically back-thinned to a thickness of about 10 μm, and then ion milled on the glass substrate side at an accelerating voltage of 5 kV using a PIPS. The crystallization microstructure was characterized by TEM. High-resolution TEM (HRTEM) was performed at 400 kV in a JEM4010 (point-to-point resolution: 0.15 nm, JEOL Co., Ltd.). Energy dispersive X-ray spectroscopy (EDXS) was applied for composition analysis of a-Si and c-Si regions.

An enlarged view of the patterns between the electrodes is shown in Figure 9. The crystallization front migrates from the negative electrode side to the positive electrode side. A needlelike morphology of c-Si was clearly observed at the interface between the fully crystallized and amorphous regions indicated by 'O' in Figure 9 as shown in Figure 10 (a). As revealed in Figures 10 (b), almost all the c-Si needles exhibit the <011>//ND orientations with respect to the a-Si film surface normal and grew the <111> and <211> directions, forming an angle of 90º between the needles. The [011] diffraction pattern taken from the needle 'A' in Figure 10 (b) showed streaks along the [111] direction, indicating that there are many stacking faults or twins normal to that direction. The a-Si region was measured to contain (2.99 ± 0.97) at.% Cu on average by EDXS measurement of five areas. In fully crystallized regions many needles were interwoven, as shown in Figure 11. The regions contained (1.63 ± 0.15) at.% Cu on average by XEDS measurements of four areas. The solubility of Cu in c-Si is negligible, and therefore, the detected Cu is believed to arise from trapped Cu solutes in the interfaces between the interwoven c-Si needles. Figure 12 (a) shows an HRTEM image also revealing the growth directions of <111> and <211> with the <011>//ND orientation, which means the {011} planes

being parallel to the surface plane. At a higher magnification (Figure 12 (b)), three {111} twins and a stacking fault can be seen. In order to consider the role of any Cu silicides on the nucleation and growth of the *c*-Si needles, the edges of the *c*-Si needles were examined. Figure 13 displays the typical edge, where Cu silicides are not observed, and instead, Si lattice image is seen. Furthermore, Cu silicides are observed even in the *a*-Si and the crystallized region within the limited field of view. The *c*-Si region at the edge contains many {111} twins and stacking faults indicated by white triangles and arrows, respectively. There seems to be also some lattice distortion in some areas, due to defects (twins or stacking faults) which are not clearly visible. As in the NiSi$_2$-mediated crystallization (Section 5.2) Cu-induced crystallization proceeds in the <111> directions with a shape of needles as shown in Figure 10(b) and Figure 12 (a). The *c*-Si needles have the <011>//ND orientations.
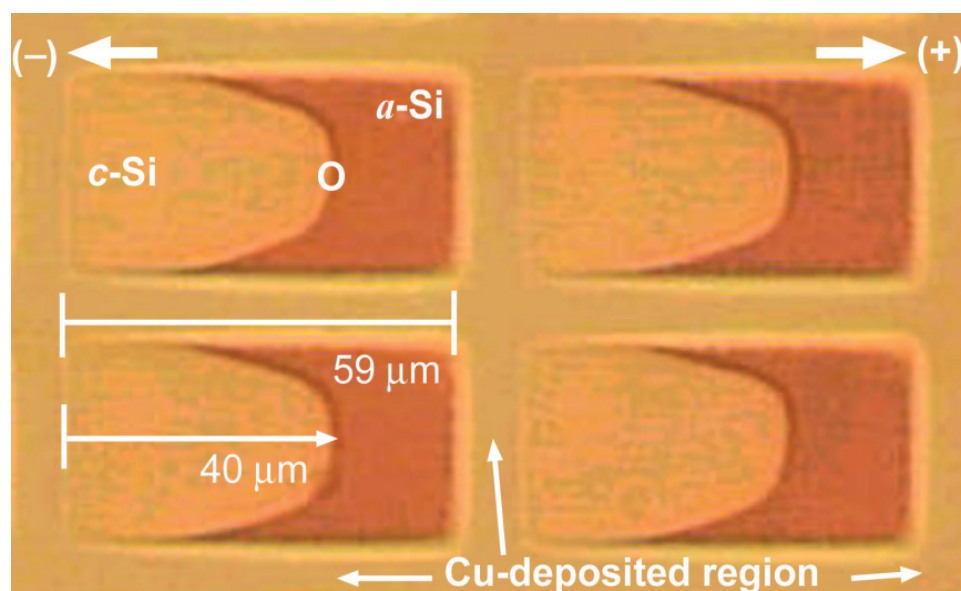
Figure 9. Optical image of patterns between electrodes [8].

Additionally, as shown in Figure 10 (b) and 12 (a), the growth occurs also in the <211> directions. At variance with the NiSi$_2$-mediated crystallization, however, as shown in Figure 13, Cu silicides are not observed at the leading edges of the *c*-Si needles, indicating that the crystallization of the Cu/*a*-Si system in this study is not mediated by any Cu silicides. Radnoczi et al. [4] suggested that Au, Sb, In and Al, which form eutectic with Si, dissolved in the a-Si film may loosen the covalent bonds in Si and make the *a*-Si even unstable, enhancing crystallization. Even though Cu is a silicide-forming metal, Cu atoms appear to enhance crystallization in a similar way to the eutectic-forming metals. Since Cu has a negligible solubility in crystalline Si [33], the Cu solute atoms are repelled by the *c*-Si. The Cu atoms will diffuse into the *a*-Si matrix, making the *a*-Si unstable, and the Si atoms will migrate into the *c*-Si side from the *a*-Si, resulting in crystallization. Diffusion of Cu atoms in *a*-Si seems to be rate-controlling. Without the application of any electric field during annealing at 500 °C (i.e., in the MILC process), the crystallization rate is reported to be 1.5–2 μm h^{-1} [12]. Copper is reported to diffuse in *a*-Si with $D > 10^{-12}$ cm^2 s^{-1} in a temperature range between 400 and 600 °C [34]. From the
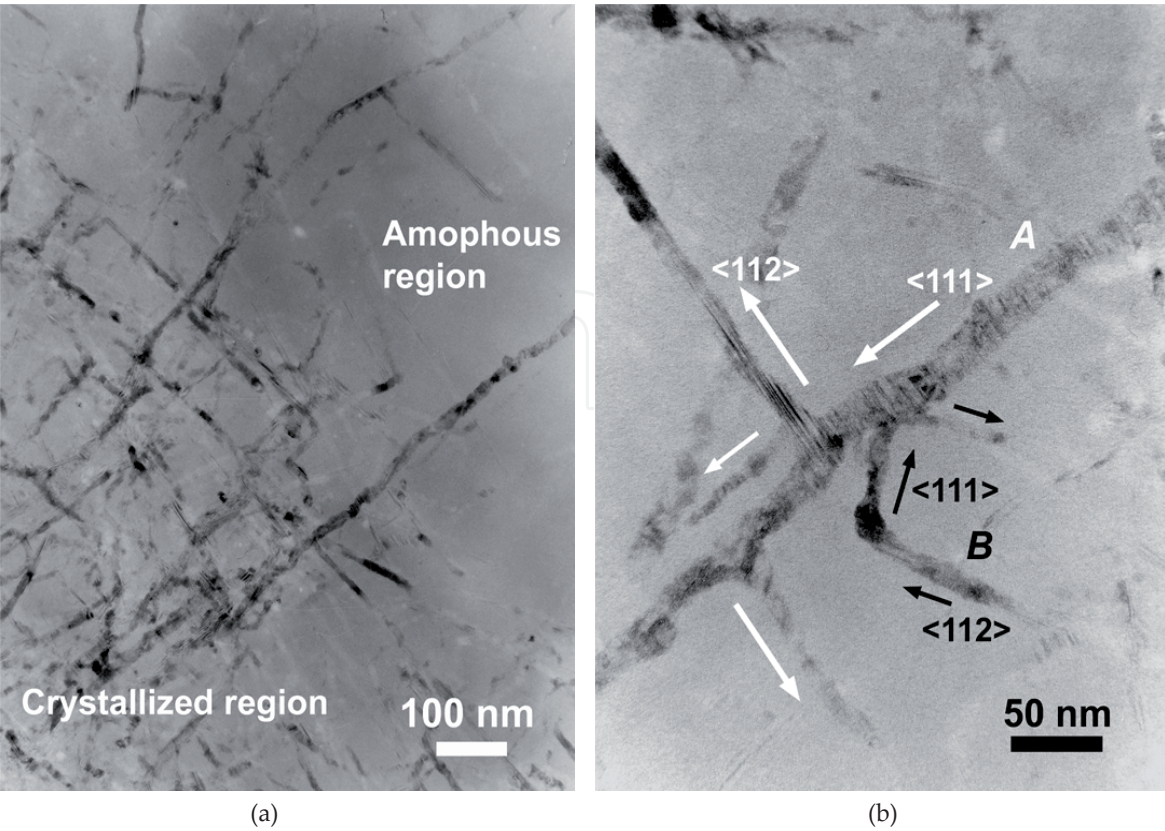
Figure 10. (a) Low magnification TEM image of partially crystallized *a*-Si revealing needlelike morphology of *c*-Si and (b) typical TEM image showing the *c*-Si needles grow in directions of <111> and <112> directions with <110>//ND orientations [8].

diffusivity value of 10^{-12} cm^2 s^{-1}, the minimum diffusion length ($\sqrt{Dt}$) is calculated to be 0.6 μm for 1 h at 500 °C. This diffusion length is in qualitative agreement with the crystallization rate obtained without any electric field in the MILC process (1.5–2 μm h^{-1}). Lee et al. [12] showed the increase in crystallization rate with an electric field of 210 V m^{-1} to 35 μm h^{-1}. Although some crystallization parameters such as pattern size, shape, and the applied electric field intensity are different, a high crystallization rate of ~40 μm h^{-1} was obtained. The crystallized pattern images in Figure 9 reveal that the macroscopic crystallization direction under an applied bias corresponds to that of electric field in the pattern.

It is suggested that the electric field in the FALC process can cause a kind of the electron wind effect (electromigration) via current flow in the pattern at the elevated temperature [35]. Choi et al. [35] propose that the electron wind effect explains the NiSi$_2$-mediated crystallization [13,14] and is limited to the diffusion of Ni in NiSi$_2$. When the current density is high enough, the momentum exchange induces the Ni atoms in NiSi$_2$ to migrate from the negative electrode side to the positive one (along the electron flow direction). In the Cu-mediated crystallization study [8], because no Cu silicides are observed at the leading edges of the *c*-Si needles, the application of the above-mentioned suggestion is not plausible. However, the electron wind effect is likely to hold for the diffusion of Cu in *a*-Si at the high temperature of 500 °C, because the resistivity of *a*-Si decreases with increasing temperature because of the exponential increase

in intrinsic carrier concentration, and at such high temperature, the electron flow in *a*-Si can cause the electron wind effect. The effect will accelerate the diffusion of Ni along the electron flow direction, and concomitantly, the crystallization rate.

(a)   (b)
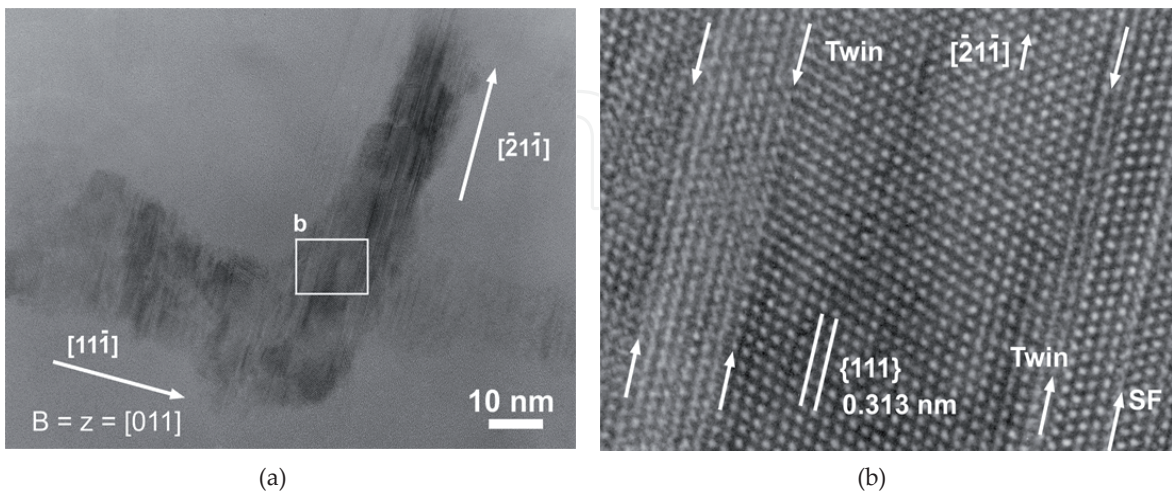
Figure 11. (a) High-resolution TEM image showing growth directions of <111> and <112> with <110>//ND orientation of *c*-Si needle. Beam direction (zone axis) is parallel to [011]. At higher magnification (b) of area indicated by white-lined box in (a), three {111} twin boundaries and one stacking fault (SF) are visible [8].
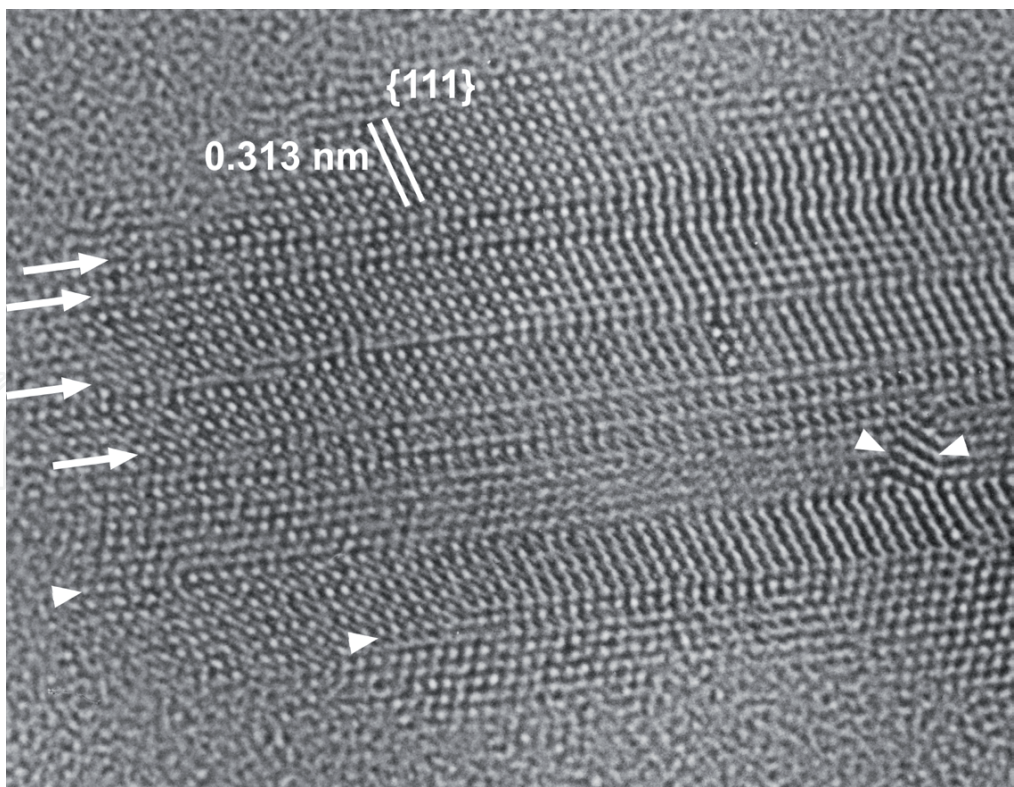
Figure 12. High-resolution image of typical edge without Cu silicides, where Si lattice image is shown. {111} twins and stacking faults are indicated by white triangles and arrows, respectively [8].

Crystallization behavior of a-Si in the Cu/a-Si bilayer (without any electric field in this case) was studied by Russell et al. [36]. They found that on heating to 175 °C, Cu$_3$Si phase appeared and subsequent heating to 485 °C resulted in the crystallization of the a-Si in the form of dendrites in the Cu$_3$Si matrix. At variance with the results of Russell et al., the matrix was observed to be still a-Si and discernible Cu silicides including Cu$_3$Si phase were not observed in the study by Lee et al. [8]. In the study by Russell et al., the thickness ratio of Cu to a-Si was determined to obtain an average composition of Cu$_{3-\delta}$Si, where δ is from 0.5 to 1. In this case the matrix (continuous phase) could become Cu$_3$Si phase. In the study by Lee et al. [8], however, the deposited Cu film (2 nm thick) is very thin with the thickness ratio to the a-Si underlying layer (80 nm) of 1:40. Therefore, as already mentioned, they could not be easily observed. They may act as heterogeneous nucleation sites for crystallization. However, the difficulty in observing the phases indicates that their nucleation density was too low and their size was too small to explain the observed, overall crystallization behavior, strongly implying that the presence of Cu solutes, not Cu silicides, enhances crystallization.

The <111> growth directions and the <011>//ND orientations observed by Lee et al. [8] are caused by anisotropic elastic properties of c-Si, although a-Si is isotropic because the strain energy can influence the crystallization rate as discussed in Sections 2 and 4. The higher strain energy will give rise to the higher crystallization rate. One of the major strain energy sources may be the thermal strain energy due to differences in thermal expansion coefficient between a-Si and the substrate glass. The thermal strain energy can influence the crystallization rate, but is not related to the directional crystallization. Since the thermal expansion coefficients of a-Si and c-Si are expected to be almost the same, the thermal strain energy between a-Si and c-Si can be negligible.

Another strain-energy may arise from the accommodation strain between a-Si and c-Si due to different structures and densities (The densities of a-Si and c-Si are measured to be 2.1 to 2.3 [37] and 2.32 to 2.34 [26], respectively). This strain energy can be anisotropic because of anisotropic elastic properties of c-Si, even though a-Si is isotropic. Since the thickness of the Si film including a-Si and c-Si is much smaller than the dimensions along the film surface, the stress in the plane normal direction (ND) is negligible, and the film is under the plane stress state. Initial Si crystallites will form in the surface layer, where the Cu concentration is highest, and they could be of a disk-shape. The surface orientation of c-Si disks is presumably random because they form from a-Si. However, their growth rates will vary with their orientations because different orientations give rise to different strain energies. According to the directed growth theory (Section 2), c-Si grows in its MxYMD <111>, resulting in the needlelike shape. If c-Si grows along the [1 1–1] direction, the growth front will be subjected to tensile stresses, which will increase with growth. When the stresses reach a point where the distance between atoms in c-Si/a-Si interface is too far to be shuffled, another <111> growth, $e.g.$, the [–1 1–1] growth, will be activated. When the <111> direction are parallel to the film surface, the c-Si needles can grow extensively and occupy large areas within the a-Si films, resulting in <110>//ND orientation (Figure 4). This may be expressed as the {110}<111> orientation.

The additional growth in the <211> directions may occur with the help of many {111} twins and stacking faults observed in the c-Si (Figure 12 (b) and Figure 13) which are certainly due

to the low stacking fault energy of Si (~50 mJ m^{-2}), even though the <211> growth directions are not favored in terms of the strain energy consideration. These {111} twins and stacking fault planes can generate steps for growth at the interface between the c-Si and a-Si, enhancing the growth in directions parallel to the twin and stacking fault planes. Because the angle between the <111> and <211> growth directions is 19.4°, we can make some errors in measurements. Even though there is some change in growth direction into <211>, the <011>//ND orientations will remain unchanged, as revealed in Figures 10 (b) and 12 (a).

5.2. Nickel-silicide mediated crystallization

Hayzelden et al. [13,14] studied the formation of buried precipitates of NiSi$_2$ in Ni-ion implanted a-Si and the subsequent NiSi$_2$-mediated crystallization of a-Si using in situ transmission electron microscopy (TEM) and high resolution TEM. a-Si thin films of 95 nm in thickness was deposited by low-pressure chemical-vapor deposition on Si substrates capped with 100 nm of thermally grown SiO$_2$. The a-Si could not crystallize from the c-Si substrate directly. Ion implantation of Ni into the a-Si was performed at an energy of 55 keV with doses of 1 and 5×10^{15} ions cm^{-2} to give a peak Ni concentration of 4×10^{20} and 2×10^{21} ions cm^{-3}, respectively, at a depth of approximately half the a-Si film thickness.

They observed that the NiSi$_2$ precipitates with CaF$_2$ structure formed in a-Si at about 400 °C, which were octahedra bounded by eight {111} faces. On the other hand, Yeh et al. [38] made a stacked structure of a-Si/Ni/SiO$_2$/Si(100) as follows: the <100>//ND oriented p-type Si wafers were chemically cleaned, followed by a dry oxidation in an atmospheric pressure chemical vapor deposition furnace to form a 3-nm-thick tunnel oxide. Subsequently, a 3.5-nm-thick Ni layer was deposited onto the tunnel oxide by electron beam evaporation. The Ni layer was capped by a 12.5-nm-thick a-Si layer deposited by sputtering. The stacked structure was, afterwards, dry oxidized at 900 °C to form a layer with control oxide on the top and NiSi$_2$ nanocrystals precipitated and embedded between tunnel oxide and control oxide. After dry oxidation, the well-separated and spherical NiSi$_2$ nanocrystals embedded in the SiO$_2$ layer are observed. The whole a-Si layer was oxidized to serve as the control oxide. The distance between NiSi$_2$ nanocrystals and the oxide/Si interface is about 10 nm indicating that about 3-nm-thick Si substrate was oxidized to contribute to about 6.5-nm-thick SiO$_2$ in addition to the 3-nm-thick tunnel oxide. The mean size and areal density of the NiSi$_2$ nanocrystals were measured to be ~ 7.6 nm and 3.3×10^{11} cm^{-2}, respectively. The nanocrystals were identified to be NiSi$_2$ phase. This indicates that the initial NiSi$_2$ crystals are spherical.

Figures 1 and 3 in [14] show that NiSi$_2$ precipitates embedded in Ni-implanted a-Si thin films appear partly rectangular and partly spherical and spherical precipitates look a little smaller than rectangular precipitates. Therefore, the initial shape of the precipitate may be spherical and the octahedral shape of NiSi$_2$ precipitates may not be intrinsic. MIC of a-Si in Section 5.1 showed that c-Si grew in its <111> directions without NiSi$_2$-mediation. This is associated with contribution of strain energy to activation energy for crystal growth at low crystallization temperatures (Section 2) or low transformation temperatures [39].

Eight {111} faces of a spherical NiSi$_2$ precipitate are likely to be the best spots for the nucleation of c-Si because the growth rate of c-Si is the highest in the <111> directions and the extremely

good lattice match between the {111} faces of NiSi$_2$ and c-Si [the lattice parameter of NiSi$_2$ (0.5406 nm) is nearly equal to that of c-Si (0.5430 nm)], resulting in the better stability of the {111} faces of NiSi$_2$ precipitate than other faces. The eight spots are shown in Figure 14. Therefore, the {111} faces are likely to grow and bound the precipitate, forming the octahedral shape during annealing. The gradual transition from spherical NiSi$_2$ to octahedral NiSi$_2$ is represented in Figure 15. In this way, a structure of a-Si/c-Si/NiSi$_2$/c-Si/a-Si may be formed in a-Si thin film. The c-Si precipitates on the left and right of NiSi$_2$ can differ in thickness. Let the left c-Si be thicker than the right c-Si. In order to distinguish the right c-Si from the left c-Si, the right c-Si is denoted by c-Si(I) and the left c-Si by c-Si(II), then the structure is expressed as a-Si/c-Si(II)/NiSi$_2$/c-Si(I)/a-Si.
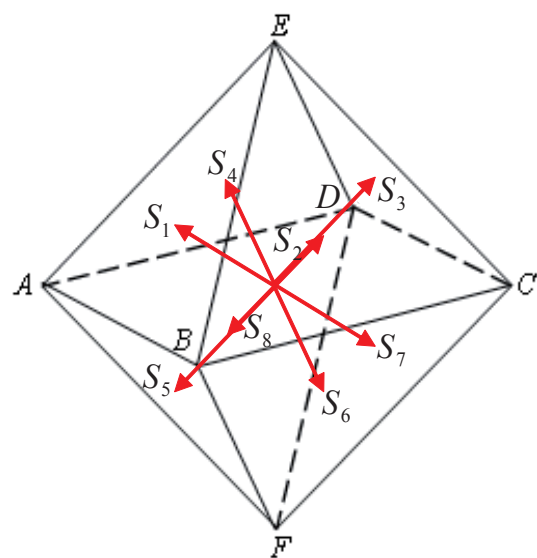
Figure 13. Octahedron bounded by {111} planes. S_1: center (c) of $\triangle$ABE, S_2: c of $\triangle$BCE, S_3: c of $\triangle$CDE, S_4: c of $\triangle$ADE, S_5: c of $\triangle$ABF, S_6: c of $\triangle$BCF, S_7: c of $\triangle$CDF, S_8: c of $\triangle$ADF. Triangles ($\triangle$) are {111} planes and edges are <110> directions. Arrows indicate <111> directions. S_1 to S_8 are on surface of one sphere.
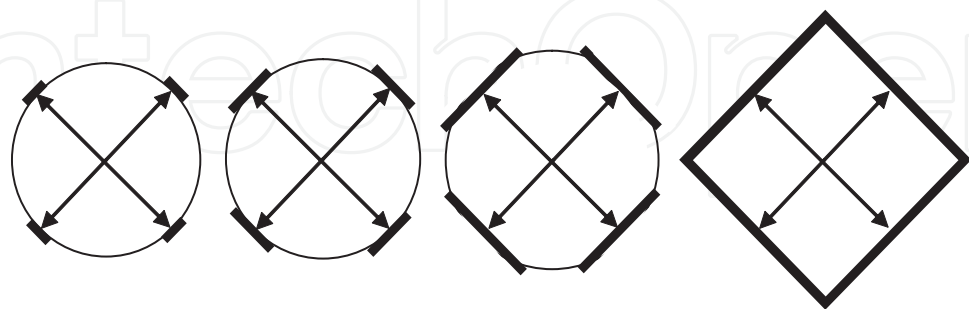


Figure 14. Schematic diagram showing gradual shape change from spherical NiSi$_2$ to octahedral NiSi$_2$. Arrows indicate <111> directions of NiSi$_2$ precipitate projected on a plane parallel to (001) plane. Black deposits indicate c-Si nucleated on {111} planes of NiSi$_2$ precipitate. Far left circle is made of S_1, S_2, S_3, S_4 or S_5, S_6, S_7, S_8 in Figure 13.

At about 500 °C, the epitaxial c-Si was nucleated on one or more of the NiSi$_2$ {111} surfaces and the c-Si needles grew in the <111> directions in the amorphous matrix with the <011>//ND

orientations (ND indicates the film surface normal). This may be expressed as {011}<111>. The NiSi$_2$ precipitates were observed to be always present at the leading edges of c-Si needles [13, 14].

The extremely good lattice match between c-Si and NiSi$_2$ and a mismatch between c-Si and a-Si give rise to stresses in c-Si near the c-Si/a-Si interface, as shown in Figure 15. Therefore, the average stress of c-Si layer in the structure of NiSi$_2$/c-Si/a-Si increases with decreasing thickness of the layer, and the molar free energy of c-Si is likely to increase with decreasing thickness. In the structure of a-Si/c-Si(II)/NiSi$_2$/c-Si(I)/a-Si, the molar free energy of c-Si(I) is likely to be higher than that of c-Si(II) and lower than that of a-Si, as shown in Figure 16. It can be seen from Figure 16 that tie lines drawn from both c-Si(I) and c-Si(II) to the NiSi$_2$ show that in equilibrium, NiSi$_2$ in contact with c-Si(I) is expected to be Si rich in comparison to NiSi$_2$ in contact with c-Si(II) [Si(I) > Si(II)].
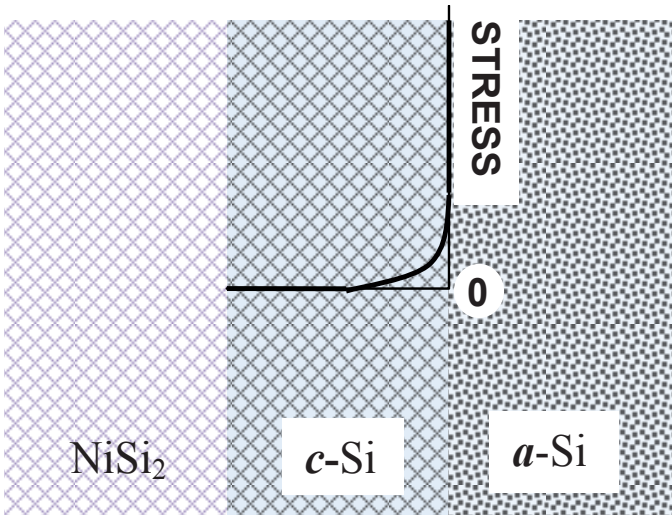

**Figure 15.** Schematic stress profile along thickness of c-Si

The driving force behind the NiSi$_2$ precipitate migration and Si crystallization, although not an equilibrium process, can be discussed by reference to an equilibrium free-energy diagram of the type shown in Figure 16. The driving force for the phase transformation is the reduction in free energy associated with the transformation of metastable a-Si to stable c-Si. Tie lines drawn from both a-Si and c-Si to the NiSi$_2$ show that in equilibrium, NiSi$_2$ in contact with a-Si is expected to be Si rich in comparison to NiSi$_2$ in contact with c-Si(I) and c-Si(II) [Si(a) > c-Si(I) > c-Si(II) in Figure 16].

The curvature of the NiSi$_2$ phase may be quite significant. For example, laser quenching has shown that the CaF$_2$ structure of NiSi$_2$ is capable of accommodating Si deficits of ~35 at.% [40]. The intersections of the tie lines with the energy axes yield the chemical potentials for Ni and Si at the c-Si/NiSi$_2$ (= NiSi$_2$/c-Si) and NiSi$_2$/a-Si interfaces. The chemical potential of the Ni atoms is lower at the NiSi$_2$/a-Si interface, whereas the chemical potential of the Si atoms is lower at the c-Si/NiSi$_2$ interface. A migrating NiSi$_2$ precipitate consuming a-Si at the leading interface and forming a trail of epitaxial c-Si [= c-Si(II)] is shown schematically in Figure 17. There is a

driving force for the forward diffusion of Ni atoms through the NiSi$_2$ and a driving force for the diffusion of Si atoms in the reverse direction through the NiSi$_2$. The consumption of a-Si at the leading edge and rejection of Si to the epitaxial c-Si trail [c-Si(II) in Figure 17] leads to the needlelike c-Si morphology. Note that the c-Si/NiSi$_2$ epitaxial interface is formed behind the migrating NiSi$_2$ precipitate.
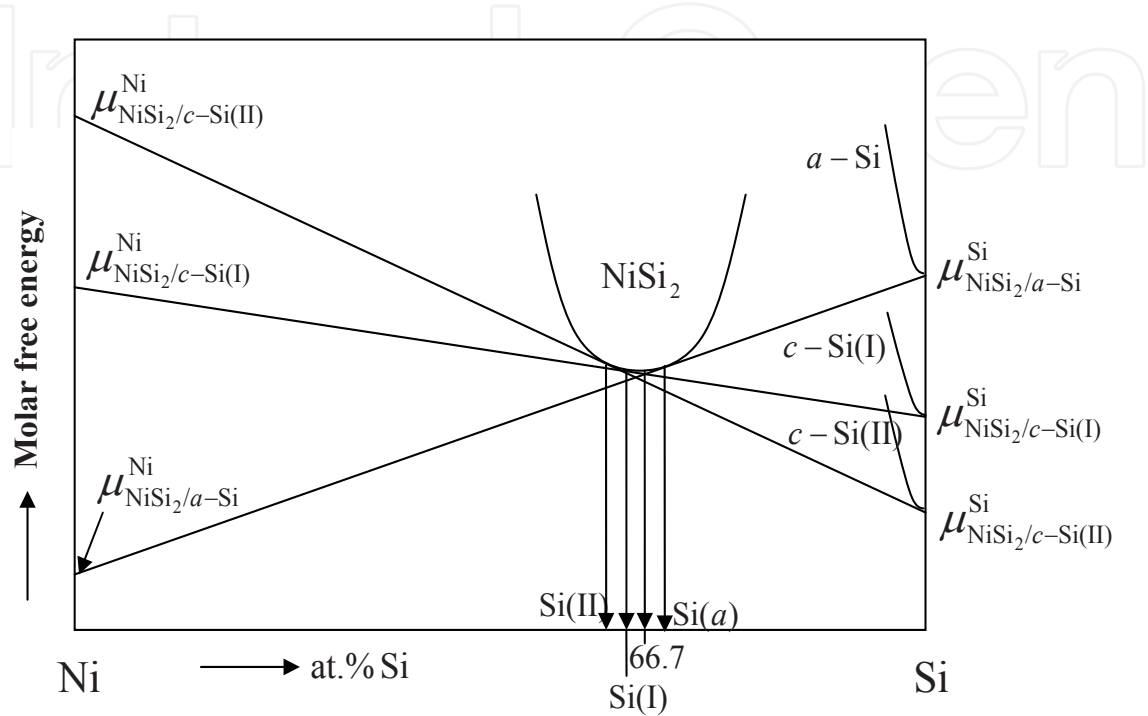
Figure 16. Schematic equilibrium molar free-energy diagram for NiSi$_2$ in contact with a-Si, c-Si(I), and c-Si(II). Si(a), Si(I), and Si(II) are Si contents in NiSi$_2$ in contact with a-Si, c-Si(I), and c-Si(II), respectively.
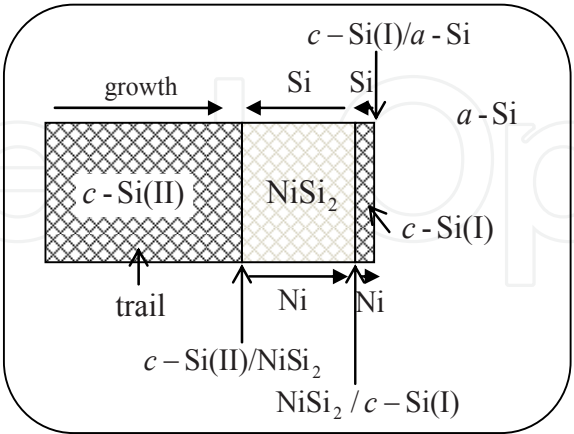
Figure 17. Schematic representation of diffusion direction of Si and Ni atoms in c-Si(II)/NiSi$_2$/c-Si(I)/a-Si system. Without c-Si(I), NiSi$_2$/c-Si(I) interface becomes NiSi$_2$/a-Si interface.

There are two limiting cases that describe the diffusional process of NiSi$_2$-mediated crystallization of a-Si. These can be the dissociative and nondissociative diffusion models. In the

dissociative model, the $NiSi_2$ layer dissociates to provide free Si for epitaxial growth at the c-Si/$NiSi_2$ interface, with new $NiSi_2$ formed at the leading $NiSi_2$/a-Si interface. In this case all the Si atoms that were originally in the $NiSi_2$ layer would be incorporated in the epitaxially grown c-Si and replaced by Si atoms from the a-Si. The diffusing species in the dissociative mechanism would be Ni atoms and the measured effective diffusivity would apply to Ni atoms. In the nondissociative model, Si atoms would simply diffuse through the $NiSi_2$ layer from the a-Si and bond to the epitaxial c-Si. The effective diffusivity would then apply to Si moving through the $NiSi_2$. In the sequential formation of Ni_2Si, NiSi, and $NiSi_2$ formed from thin-film diffusion couples of around 100 nm of Ni on Si, Ni is known to be the fast-diffusing species [41-43].

Figure 16 also shows that the chemical potential of the Ni atoms, μ^{Ni}, is higher at the $NiSi_2$/c-Si(II) interface, or the c-Si(II)/$NiSi_2$ interface, than at the $NiSi_2$/c-Si(I) interface, whereas the chemical potential of the Si atoms, μ^{Si}, is lower at the $NiSi_2$/c-Si(II) interface than at the $NiSi_2$/c-Si(I) interface. Therefore, the $NiSi_2$ layer dissociates to provide free Si for epitaxial growth at the c-Si(II)/$NiSi_2$ interface, with excess Ni at the c-Si(II)/$NiSi_2$ interface diffusing through $NiSi_2$ into the $NiSi_2$/c-Si(I) interface, interacting with c-Si(I) to form $NiSi_2$, resulting in depletion of Si in c-Si(I). The depleted Si is replaced by Si from a-Si because the molar free energy of c-Si(I) is lower than that of a-Si. In this way, the Ni atoms diffuses from the c-Si(II)/$NiSi_2$ interface through $NiSi_2$ and c-Si(I) into the c-Si(I)/a-Si interface, whereas the Si atoms effectively diffuse from the c-Si(I)/a-Si interface through the Si(I) and NiSi2 layers into the c-Si(II)/$NiSi_2$ interface. This process eventually makes the $NiSi_2$ precipitate migrate rightward consuming a-Si at the leading interface [c-Si(I)/a-Si] to form a trail of epitaxial c-Si(II) as shown in Figure 17. As this process proceeds, the c-Si(II) layer gradually thicken and the c-Si(I) layer gradually thin to a few layers, which is stable enough to survive because of the extremely good lattice match between $NiSi_2$ and c-Si. Consequently, the consumption of a-Si at the leading edge and rejection of Si to the epitaxial c-Si(II) trail take place and leads to the needlelike c-Si forming behind the migrating $NiSi_2$ precipitate.

The reason why during crystallization, the shape of the $NiSi_2$ precipitates at the leading edges of the c-Si needles assume the thin plate shape, whereas the leading edges of the c-Si needles are not flat (Figure 9) can be attributed to the extent of elastic anisotropy between $NiSi_2$ and c-Si. Zener's anisotropy factor, $A=2(S_{11}-S_{12})/S_{44}$, is used to denote the extent of elastic anisotropy of cubic materials. When the ratio A is unity, the elastic properties are isotropic, but they can deviate from isotropy in two ways, by A being either greater than or less than unity. A = 1.83 for $NiSi_2$ ($S_{11} = 0.01219$, $S_{12} = -0.00505$, $S_{44} = 0.01887$ GPa^{-1} [44]) and A = 1.56 for c-Si (Section 4). Thus, the extent of elastic anisotropy of $NiSi_2$ is higher than that of c-Si, implying that the {111} planes of $NiSi_2$ have higher potential of existence than the {111} planes of c-Si. The higher Young's modulus reflects the higher bonding strength. Therefore, the region surrounding the interface edge is strained, which in turn gives rise to crystallization along the interface plane as well as along the needle axis. In this way, the c-Si needles fan out during its growth (Figure 18), and simultaneously, the $NiSi_2$ precipitates become thinner. As the interface area increases, the accommodation strain increases to a point such that coherency between the two crystals cannot be maintained, resulting in dissociation of the $NiSi_2$ crystal into a few smaller crystallites. These smaller precipitates continue to mediate the growth [14]. Because the growth is

mediated by the NiSi$_2$ whose {111} planes have higher potential of existance than that of c-Si, the {011}<111>-oriented growth for the NiSi$_2$-mediated crystallization remains without growth in other directions (e.g., <211> for the Cu-enhanced crystallization).

Diffusion of Ni through c-Si to reach the a-Si in Figure 18 is consistent with previous experiments on Ni-assisted Si epitaxy. Erokhin et al. [45] deposited a film of Ni on a c-Si/a-Si structure and observed Ni diffusion to the c-Si/a-Si interface to form NiSi$_2$ after annealing for 43 h at 350 °C. Decomposition of NiSi$_2$ at the NiSi$_2$/c-Si interface with Ni diffusion into the a-Si was suggested as a mechanism for Si crystallization. This is in good agreement with the model of dissociative diffusion of Ni from the NiSi$_2$/c-Si interface to leave an abrupt planar interface. Low-temperature crystallization has also been reported following Ni deposition on hydrogenated a-Si (a-Si:H) [43]. The silicidation process of Ni/a-Si:H on a fused silica substrate was investigated by in situ electrical resistance measurements and x-ray diffraction and Rutherford backscattering spectroscopy [7]. It was reported that NiSi formed first at 330 °C followed by NiSi$_2$ at 420 °C. Crystallization of the a-Si:H occurred at approximately 480 °C and it was suggested that such crystallization resulted from heterogeneous nucleation of c-Si on the NiSi$_2$ phase.
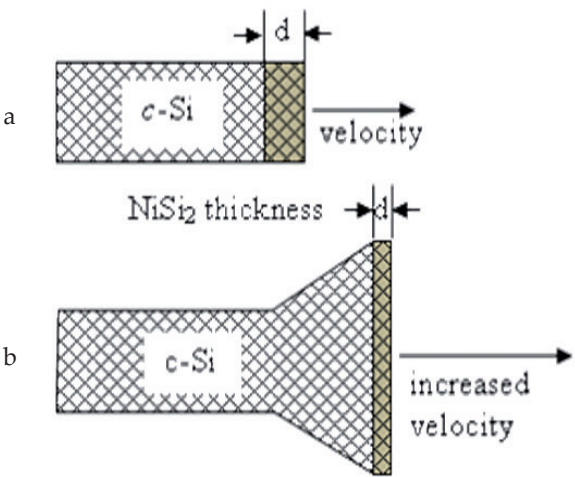
Figure 18. Schematic representation of diffusion-controlled growth of silicide-mediated crystallization of Si [14].

In Summary, the NiSi$_2$-mediated crystallization of a-Si can occur through the following processes. The initial shape of the NiSi$_2$ precipitated in the a-Si thin film is likely to be spherical and transforms into the octahedral shape during annealing because of the extremely good lattice match between c-Si and NiSi$_2$ and preferential growth of c-Si along its <111> directions. Crystalline silicon layers nucleated on the {111} faces of NiSi$_2$ precipitates can differ in thickness. This brings about a structure of a-Si/c-Si(II)/NiSi$_2$/c-Si(I)/a-Si with c-Si(II) layer being thicker than c-Si(I) layer. The c-Si(I) layer is more stressed than the c-Si(II) layer, and so the molar free energy of c-Si(I) is higher than that of c-Si(II), but lower than that of metastable a-Si. Therefore, in this system, the Ni atoms diffuse from the c-Si(II)/NiSi$_2$ interface through NiSi$_2$ into the c-Si(I)/a-Si interface, whereas the Si atoms diffuse from the c-Si(I)/a-Si interface

through $NiSi_2$ into the c-Si(II)/$NiSi_2$ interface, and the depleted Si atoms in the c-Si(I) layer are replaced by a-Si. This process eventually makes the $NiSi_2$ precipitate migrate consuming a-Si at the leading interface [c-Si(I)/a-Si interface] and forming the needlelike trail of epitaxial c-Si(II). Consequently, the c-Si(II)/$NiSi_2$ epitaxial interface is formed behind the migrating $NiSi_2$ precipitate. Migrating $NiSi_2$ precipitates resulted in crystallization of Si at temperatures as low as 484 °C, which is ~200 °C lower than the intrinsic temperature required for crystallization of pure a-Si. The $NiSi_2$-mediated crystallization rate is controlled by diffusion through the migrating $NiSi_2$ precipitates.

6. Conclusions

1. The solid-phase crystallization of an amorphous material needs the activation energy. The energy is usually supplied in the form of thermal energy by increasing the temperature of the material. When the nucleation occurs, the strain energy develops in the amorphous matrix as well as in the crystalline nuclei, or crystallites. The strain energy is the highest in the stable/metastable interface region in the highest Young's modulus directions of the stable phase. Therefore, the growth rate of the crystallites is the highest in the metastable phase along the maximum Young's modulus directions of the crystallites because the activation barrier can be surmounted by the strain energy when the thermal energy is not high enough to surmount the barrier. The strain energy is likely to give rise to inhomogeneous growth rates of crystallites due to their elastic anisotropy, if any. This directed crystallization theory can explain the following results.

2. The solid-phase epitaxial growth rate of c-Si from a-Si by bending the bar-shaped Si(001) wafers (p type, 1 ohm cm, 0.84 mm thickness) whose both sides were implanted to create 280–nm-thick amorphous surface layers, were elastically bent using a three-point bending system at about 540 °C. One side of the elastically bent specimen is approximately under a uniaxial tensile stress state and the other side under a uniaxial compressive stress state, in which the stress ranged from –0.55 GPa (compressive) to 0.55 GPa (tensile). The measured crystallization rate as a function of applied stress showed that the rate in the tension side was higher than that in the compression side. The result is understood because the a-Si film on the tension side of the sample could be more stressed than that on the compression side. On the other hand, at temperatures of 530–550 °C and hydrostatic pressures up to 3.2 GPa, the solid-phase epitaxial growth rate of self-implanted Si(100) was enhanced by up to a factor of 5 over that at 1 atmosphere pressure (≈ 0.1 MPa). This result appears to contradict the non-hydrostatic stress effect of the bent specimen. The crystallization of a-Si results in a decrease in volume. Therefore, a hydrostatic compression is expected to accelerate crystallization. However, the stress of -0.55 GPa is too low to yield effective densification.

3. Evaporated a-Si film crystallizes into dendrite forms with dendrite arms in the <111> directions at low annealing temperatures. As the annealing temperature increases the a-Si film crystallized with increasingly equiaxed grains and random textures. The results

are compatible with the directed crystallization theory because the strain energy contribution to the activation energy decreases with increasing annealing temperature and in turn the isotropic crystallization rate increases. The crystallization temperature decreases with increasing purity of a-Si films.

4. The solidus temperature of $Si_{0.47}Ge_{0.53}$ is 1095 °C, which is lower than the melting point of Si, 1414 °C. Therefore, at an annealing temperature of 600 °C, crystallization of a-$Si_{0.47}Ge_{0.53}$ was dominated by the thermal energy unlike Si. The aspect ratio of crystallites decreased with increasing content of Ge. This also reflects an increase in thermal energy contribution with increasing Ge content.

5. The crystallization behavior of a Cu-deposited a-Si/glass sample annealed at 500°C for 1 h with an electric field of 180V/cm has shown that the Si crystallites grow in the <111> and <112> directions with the <110>//ND orientation, assuming a needlelike shape. No Cu silicides are observed, and it seems that the Cu atoms in the a-Si film make the a-Si unstable, resulting in crystallization at the relatively low temperature. The growth directions of <111> and the <110>//ND orientations are compatible with the directed crystallization theory. The <112> directions can be possible with the help of many {111} twins and stacking faults in c-Si.

6. The $NiSi_2$-mediated crystallization of a-Si can occur through the following processes. The initial shape of the $NiSi_2$ precipitated in the a-Si thin film is likely to be spherical and transforms into the octahedral shape during annealing because of the extremely good lattice match between c-Si and $NiSi_2$ and preferential growth of c-Si along its <111> directions. Crystalline silicon layers nucleated on the {111} faces of $NiSi_2$ precipitates can differ in thickness. This brings about a structure of a-Si/c-Si(II)/$NiSi_2$/c-Si(I)/a-Si with c-Si(II) layer being thicker than c-Si(I) layer. The c-Si(I) layer is more stressed than the c-Si(II) layer, and so the molar free energy of c-Si(I) is higher than that of c-Si(II), but lower than that of metastable a-Si. Therefore, in this system, the Ni atoms diffuse from the c-Si(II)/$NiSi_2$ interface through $NiSi_2$ into the c-Si(I)/a-Si interface, whereas the Si atoms diffuse from the c-Si(I)/a-Si interface through $NiSi_2$ into the c-Si(II)/$NiSi_2$ interface, and the depleted Si atoms in the c-Si(I) layer are replaced by a-Si. This process eventually makes the $NiSi_2$ precipitate migrate consuming a-Si at the leading interface [c-Si(I)/a-Si interface] and forming the needlelike trail of epitaxial c-Si(II).

Acknowledgements

Author details

Dong Nyung Lee* and Sung Bo Lee

*Address all correspondence to: dnlee@snu.ac.kr

Department of Materials Science and Engineering, Seoul National University, Seoul, Republic of Korea

References

[1] Matsuyama T, Terada N, Baba T, Sawada T, Tsuge S, Wakisaka K, Tsuda S. High quality polycrystalline thin film prepared by a solid phase crystallization method. Journal of Non-Crystalline Solids 1996;198–200 940–944.

[2] Song I-H, Kim C-H, Nam W-J, Han M-K. A poly-Si thin film transistor fabricated by new excimer laser recrystallization employing floating active structure. Current Applied Physics 2002;2 225–228.

[3] Hultman L, Robertsson A, Hentzell HTG, Engström I, Psaras PA. Crystallization of amorphous silicon during thin-film gold reaction. Journal of Applied Physics 1987;62 3647–3655.

[4] Radnoczi G, Robertsson A, Hentzell HTG, Gong SF, Hasan MA. Al induced crystallization of a-Si. Journal of Applied Physics 1991;69 6394–6399.

[5] Gong SF, Hentzell HTG, Robertsson AE, Hultman L, Hörnström S-E, Radnoczi G. Al-doped and Sb-doped polycrystalline silicon obtained by means of metal induced crystallization. Journal of Applied Physics 1987;62 3726–3732.

[6] Nemanich RJ, Tsai CC, Thompson MJ, Sigmon TW. Interference enhanced Raman scattering study of the interfacial reaction of Pd on a-Si:H. Journal of Vacuum Science & Technology. 1981;19 685–688.

[7] Kawazu Y, Kudo H, Onari S, Arai T. Low-temperature crystallization of hydrogenated amorphous silicon induced by nickel suicide formation. Japanese Journal of Applied Physics 1990 29; 2698–2704.

[8] Lee SB, Choi D-K, Lee DN. Transmission electron microscopy observations of Cu-induced directional crystallization of amorphous silicon Journal of Applied Physics 2005 98;114911–114917.

[9] Song K-S, Park S-H, Jun S-I. Choi D-K. Crystallizaion of the amorphous silicon using field aided lateral crystallization. In: Lee DN. (ed.) Proceedings of the Annual Meeting of the Research Center for Thin Film Fabrication and Crystal Growth of Ad-

vanced Materials (RETCAM), Seoul National University, Seoul, Korea; 1997. pp. 144–150.

[10] Jang J, Oh JY, Kim SK, Choi YJ, Yoon SY, Kim CO. Electric-field-enhanced crystallization of amorphous silicon. Nature 1998;395 481–483.

[11] Park S-H, Jun S-I, Song K-S, Kim C-K, Choi D-K. Field Aided Lateral Crystallization of Amorphous Silicon Thin Film. Japanese Journal of Applied Physics 1999;38 L108–L109.

[12] Lee J-B, Lee C-J, Choi D-K. Influences of various metal elements on field aided lateral crystallization of amorphous silicon films. Japanese Journal of Applied Physics 2001;40 6177–6181.

[13] Hayzelden C, Batstone JL, Cammarata RC. ln Situ transmission electron microscopy studies of silicide-mediated crystallization of amorphous silicon. Applied Physics Letters 1992;60 225–227.

[14] Hayzelden C, Batstone JL. Silicide formation and silicide-mediated crystallization of nickel-implanted amorphous silicon thin films. Journal of Applied Physics 1993;73 8279–8289.

[15] Anderson RM. Microstructural analysis of evaporated and pyrolytic silicon thin films. Journal of Electrochemical Society 1973;120 1540–1546.

[16] Chao SS, Gonzalez-Hernandez J, Martin D, Tsu R. Effects of substrate temperature on the orientation of ultrahigh vacuum evaporate Si and Ge films. Applied Physics Letters 1985;46 1089–1091.

[17] Gonzalez-Hernandez J, Martin D, Chao SS, Tsu R. Crystallization temperature of ultrahigh vacuum deposited silicon films. Applied Physics Letters 1980;45 101–103.

[18] Haji L, Joubert P, Economou NA, Mode of growth and microstrucure of polycrystalline silicon obtained by solid-phase crystallization of an amorphous silicon film, Journal of Applied Physics 1994;75 3944-3952.

[19] Hwang C-W, Ryu M-K, Kim K-B, Lee S-C, Kim C-S. Solid phase crystallization of amorphous $Si_{1-x}Ge_x$ films deposited on SiO_2 by molecular beam epitaxy. Journal of Applied Physics 1995;77 3042–3047.

[20] Lee DN. crystallization of amorphous silicon deposits on glass substrates. Advanced Materials Research 2007;26-28 623–628.

[21] Lee DN. Solid-phase crystallization of amorphous Si films on glass and Si wafer. Journal of Physical Chemistry of Solids 2011;72 1330–1333.

[22] Timoshenko SP, Goodier JN. Theory of Elasticity, 3rd edition, McGraw-Hill Kogakusha, Ltd., Tokyo, 1970, Section 28.

[23] Aziz MJ, Sabin PC, Lu G-Q. The activation strain tensor: nonhydrostatic stress effects on crystal-growth kinetics. Physical Review B 1991;44 9812–9816.

[24] Witvrouw A, Spaepen F. Viscosity and elastic constants of amorphous Si and Ge. Journal of Applied Physics 1993;74 7154–7161.

[25] Lu GQ, Nygren E, Aziz MJ, Turnbull D, White CW. Pressure enhanced solid phase epitaxy of silicon. Applied Physics Letters 1989;54 2583–2586.

[26] Weast RC (ed.) Handbook of Chemistry and Physics, 49th ed., The Chemical Rubber Co. Cleveland, OH, 1968, p. B-242.

[27] Custer JS, Thompson MO, Jacobson DC, Poate JM, Roorda S, Sinke WC, Spaepen F. Density of amorphous Si. Applied Physics Letters 1994;64 437–439.

[28] Fabian J, Allen PB. Thermal expansion and Grüneisen parameters of amorphous silicon: a realistic model calculation. Physical Review Letters 1997;79 1885–1888.

[29] Jiang X, Goranchev B, Schmidt K, Grünberg P, Reichelt K. Mechanical Properties of a-Si:H films studied by Brillouin scattering nanoindenter. Journal of Applied Physics 1990; 67 6772–6778.

[30] Lee DN. Elastic properties of thin films of cubic system. Thin Solid Films 2003;434 183–189.

[31] Lee DN. Corrigendum to "Elastic properties of thin films of cubic system" [Thin Solid Films 2003;434 183–189]. Thin Solid Films 2012;520 3708.

[32] McSkimin HJ. Measurement of elastic constants at low temperatures by means of ultrasonic waves- Data for silicon and germanium single crystals, and for fused silica. Journal of Applied Physics 1953;24 988–997.

[33] Data from SGTE alloy databases (revised 2004).

[34] Elliman RG, Gibson JM, Jacobson DC, Poate JM, Williams JS. Diffusion and precipitation in amorphous Si. Applied Physics Letters1985;46 478–480.

[35] Choi D-K, Kim H-C, Kim Y-B. Mechanism of field-aided lateral crystallization of amorphous silicon. Applied Physics Letters 2005;87 063108.

[36] Russell SW, Li J, Mayer JW. *In situ* observation of fractal growth during *a*-Si crystallization in a Cu_3Si matrix. Journal of Applied Physics 1991;70 5153–5155.

[37] Haage T, Schmidt UI, Fath H, Hess P, Schröder B, Oechsner H. Density of glow discharge amorphous silicon films determined by spectroscopic ellipsometry. Journal of Applied Physics 1994;76 4894–4896.

[38] Yeh PH, Yu CH, Chen LJ, Wu HH, Liu PT, Chang TC. Low-power memory device with $NiSi_2$ nanocrystals embedded in silicon dioxide layer. Applied Physics Letters 2005;87 193504 3pp.

[39] Lee DN, Han HN. Orientation relationships between precipitates and their parent phases in steels at low transformation temperatures (review). Journal of Solid Mechanics and Materials Engineering 2012; 6 323–338. Doi: 10.1299/jmmp.6.323.

[40] Tung RT, Gibson JM, Jacobson DC, Poate JM. Liquid phase growth of epitaxial Ni and Co silicides. Applied Physics Letters 1983;43 476–478.

[41] Chu WK, Lau SS, Mayer JW, Müller H, Tu KN. Implanted noble gas atoms as diffusion markers in silicide formation. Thin Solid Films 1975;25 393–402.

[42] Scott DM, Nicolet M-A. Implanted oxygen in NiSi formation. Physica Status Solidi A 1981;66 773–778.

[43] d'Heurle F, Petersson S, Stolt L, Strizker B. Diffusion in intermetallic compounds with the CaF2 structure: a marker study of the formation of NiSi2 thin films. Journal of Applied Physics 1982;53 5678–5681.

[44] Malegori G, Miglio L. Elastic properties of $NiSi_2$, $CoSi_2$, and $FeSi_2$ by tight-binding calculations. Physical Review B 1993;48 9223–9230.

[45] Erokhin YN, Grötzschel R, Oktyabrsky SR, Roorda S, Sinke W, Vyatkin AF. Mesotaxy by nickel diffusion into a buried amorphous silicon layer. Materials Science Engineering B 1992;12 103–106.